Differential Drag-Based Multiple Spacecraft Maneuvering and On-Line Parameter Estimation Using Integral Concurrent Learning

Camilo Riano-Rios[a,*], Riccardo Bevilacqua[a,*], Warren E. Dixon[a]

[a] *University of Florida, 939 Sweetwater Dr., Gainesville, FL*

Abstract

In this paper, a set of low Earth orbiting spacecraft consisting of multiple chasers and a single cooperative or unknown target, is considered for rendezvous and along-orbit formation maneuvers. Each maneuverable spacecraft can change its experienced atmospheric drag acceleration by extending/retracting dedicated surfaces. A Lyapunov-based adaptive controller is designed using an Integral Concurrent Learning (ICL)-based adaptive update law and the Schweighart-Sedwick equations of relative motion to regulate the in-plane relative states of each target-chaser pair. The controller is designed to compensate for uncertainties in atmospheric density, drag or ballistic coefficient and the velocity relative to the atmosphere of each spacecraft in the fleet. When the system is sufficiently excited, the controller also provides estimation of the uncertain parameters. Numerical simulations using nonlinear dynamics for each spacecraft and the NRLMSISE-00 atmospheric density model, are conducted to validate the performance of the controller.

Keywords: Differential Drag, Adaptive, Atmospheric Density, Drag Coefficient, Rendezvous, Formation, Integral Concurrent Learning.

*Corresponding author

Email addresses: crianorios@ufl.edu (Camilo Riano-Rios), bevilr@ufl.edu (Riccardo Bevilacqua)

1. Introduction

As the interest in exploiting natural forces for orbital maneuvering increases due to its potential for propellant cost savings, the use of these forces to maneuver fleets with several spacecraft for missions in Low Earth Orbit (LEO) has increasing interest. Atmospheric drag is the greatest non-gravitational force acting on a spacecraft in LEO, and the difference in acceleration due to drag (differential drag) between two spacecraft has been used to perform relative maneuvering. The differential drag has been successfully used in the ORBCOMM constellation of satellites to save propellant in thruster-based formation keeping maneuvers [1], and in the large fleet of Planet Labs satellites for propellant-less phasing maneuvers along the same orbit [2].

The introduction of differential drag for formation keeping control dates back to 1989, when the Clohessy-Wiltshire (CW) linear equations for relative motion between two spacecraft was used to design an algorithm to control the relative in-plane motion by transforming the dynamics into a double integrator and a harmonic oscillator. This model was used to obtain a closed-form solution under the assumption of constant differential drag and a control algorithm was developed to regulate the states with a discrete input [3].

Atmospheric drag and lift were exploited to control in-plane and out-of-plane motion between two spacecraft in [4]. Independent control algorithms were developed for the in-plane and out-of-plane motion using differential drag and lift, respectively. Based on the required inputs, an algorithm computed the orientation of a flat plate attached to each spacecraft. The Schweighart-Sedwick (SS) linear equations for relative motion that include the J_2 perturbation [5] were used to develop a discrete control algorithm for rendezvous maneuvers based on closed form solutions in [6].

A Lyapunov-based control strategy was implemented in [7] to achieve spacecraft rendezvous using differential drag. The in-plane unstable SS dynamic model was initially stabilized using a Linear Quadratic Regulator (LQR) and then a Lyapunov-based controller was designed using the error between the

relative states and the stabilized dynamics, the control commands were also restricted to discrete values. An adaptive capability to change controller parameters depending on the critical value of differential drag was also included. In [8], the attitude of a spacecraft was used to change the experienced drag instead of dedicated actuators for drag surfaces. An LQR controller was designed to drive the system to a desired relative motion using a state space representation of the error. The control command was then used to compute a normal vector to the drag surface attached to the body that served as reference for an attitude determination and control system (ADCS).

Research has also been conducted to include multiple spacecraft in simultaneous relative maneuvers with respect to a single target. A centralized heuristic control logic was used in [6] to give priority to a specific chaser in the fleet, then the target set its control command to meet the control requirements of the prioritized chaser. Only chasers that required the same sign for their corresponding inputs were able to satisfy the control command simultaneously, while the others remain with zero differential drag until a new priority was established. In [9], the formulation of an optimization problem was presented to find the minimum time required to achieve rendezvous with any number of spacecraft by using an augmented state space representation. Simulations with 2, 5 and 12 spacecraft were conducted using linearized dynamics.

An adaptive sliding mode strategy was used in [10] to control the relative dynamics using a continuous differential drag input. The controller was simulated for formation keeping as well as reconfiguration maneuvers using two spacecraft. A heuristic algorithm for multiple spacecraft was developed and applied to an along-orbit formation keeping maneuver with four spacecraft. In this algorithm, each chaser changes its drag acceleration to satisfy its control command and the target changes its drag acceleration each orbit to sequentially satisfy the differential drag requirement of each chaser.

One of the main challenges of differential-drag based relative maneuvers is that the controller is required to be robust to uncertainty in parameters such as atmospheric density and the drag coefficient, which are required to compute the

drag acceleration experienced by a spacecraft. Models for atmospheric density such as the 1976 U.S Standard [11], Harris-Priester [12] and NRLMSISE-00 [13], among others, are commonly used to estimate the local density. Some of the more complex density models include spacecraft position, date, time, and solar and geomagnetic indices as input parameters. Alternatively, the drag coefficient is calculated using theoretical [14, 15] or numerical models for simple spacecraft shapes [16, 17]. However, the level of uncertainty is still significant even when using complex models [18].

Lyapunov-based adaptive control techniques have been successfully used in the past for differential-drag based relative maneuvering, achieving state regulation despite some system uncertainties [7, 19]. However, the adaptive update laws did not ensure convergence of the parameter estimates to their true values. Various adaptive controllers have been developed under the assumption of persistence of excitation (PE) [20, 21, 22] to achieve simultaneous error regulation and system identification. Nevertheless, this can only be ensured under persistent excitation (PE) which cannot be guaranteed and is difficult to verify on-line for general nonlinear systems. A concurrent learning (CL) adaptive update law was developed in [23, 24] to achieve state regulation or tracking and on-line parameter estimation while relaxing the PE requirement, which became a verifiable condition of finite excitation, assuming the highest order states were measurable. A modification to the CL update law, called integral concurrent learning (ICL), was presented in [25, 26] to achieve estimation convergence without measuring the highest order states.

In this paper, a Lyapunov-based adaptive control algorithm that incorporates an ICL update law is developed. Unlike the preliminary efforts in [19] where only regulation of the in-plane relative states between chaser and target in LEO was ensured, the result in this paper shows simultaneous state regulation and online identification of uncertain parameters, including the drag or ballistic coefficient, the magnitude of the spacecraft-atmosphere relative velocity and the atmospheric density. The developed controller exploits the use of an LQR control law to address the problem of regulating the four in-plane states

of the SS dynamics with a single input. This input is then modified to include an adaptive term that provides the adaptation and online estimation capability. The use of a linearly parameterizable time-varying atmospheric density model enables the development of an ICL-based adaptive update law that also estimates this highly uncertain parameter online. The controller designed in this paper is intended to provide robustness to uncertainty as well as an improved insight about the uncertain parameters as compared to *a priori* information, without relying on complex models or computationally expensive operations.

Numerical simulations for rendezvous and along-orbit formation are performed using a fleet of multiple chasers maneuvering with respect to a cooperative and an unknown target, respectively. Each maneuverable spacecraft is assumed to be equipped with the Drag Maneuvering Device (DMD) developed at the University of Florida ADvanced Autonomous Multiple Spacecraft (ADAMUS) laboratory.

The paper is organized as follows: Section 2 presents the dynamic models used for control design and numerical simulations, Section 3 shows the control design, Section 4 presents the corresponding stability analysis, Section 5 explains the multiple spacecraft rendezvous and along-orbit formation maneuvers and Sections 6 and 7 show the numerical simulations and conclusions, respectively.

2. Dynamics Modeling

2.1. Spacecraft Relative Dynamics

In LEO, the dynamics of a spacecraft can be modeled considering the gravitational influence of the Earth including J_2 and the non-gravitational influence of atmospheric drag and lift. In the Earth Centered Inertial (ECI) coordinate system, the acceleration of the spacecraft can be written as

$$\ddot{x} = -\frac{GM_{\oplus}}{r^3}x + \frac{3}{2}\left(\frac{J_2 GM_{\oplus}R_{\oplus}^2}{r^4}\right)\left(\frac{x}{r}\left(\frac{5z^2}{r^2}-1\right)\right) + \ddot{r}_{D,x} + \ddot{r}_{L,x} \qquad (1)$$

$$\ddot{y} = -\frac{GM_{\oplus}}{r^3}y + \frac{3}{2}\left(\frac{J_2 GM_{\oplus}R_{\oplus}^2}{r^4}\right)\left(\frac{y}{r}\left(\frac{5z^2}{r^2}-1\right)\right) + \ddot{r}_{D,y} + \ddot{r}_{L,y} \tag{2}$$

$$\ddot{z} = -\frac{GM_{\oplus}}{r^3}z + \frac{3}{2}\left(\frac{J_2 GM_{\oplus}R_{\oplus}^2}{r^4}\right)\left(\frac{z}{r}\left(\frac{5z^2}{r^2}-3\right)\right) + \ddot{r}_{D,z} + \ddot{r}_{L,z} \tag{3}$$

where $\ddot{\boldsymbol{r}}_{\boldsymbol{D}} = [\ddot{r}_{D,x}, \ddot{r}_{D,y}, \ddot{r}_{D,z}]^T$ and $\ddot{\boldsymbol{r}}_{\boldsymbol{L}} = [\ddot{r}_{L,x}, \ddot{r}_{L,y}, \ddot{r}_{L,z}]^T$ are the accelerations due to atmospheric drag and lift expressed in the ECI coordinate system, respectively. In (1)-(3), G is the universal gravitational constant, $\boldsymbol{r} = [x, y, z]^T$ is the ECI position of the spacecraft, J_2 is the coefficient that represents the second order harmonic of gravitational potential field of the Earth, and $M_{\oplus}$ and $R_{\oplus}$ are the mass and radius of the Earth, respectively.

Assumption 1. Each maneuverable spacecraft is ram-aligned and all objects are in circular LEO, the inter-spacecraft distance is small compared to the radius of the orbit.

Under Assumption 1, the relative motion between any chaser and the target can be expressed in the Local-Vertical/Local-Horizontal (LVLH) coordinate system (Figure 1) using the SS dynamic model that includes the influence of J_2 perturbation as follows:

$$\Delta\ddot{x} = 2(\Omega c)\Delta\dot{y} + \left(5c^2 - 2\right)\Omega^2\Delta x + u_x \tag{4}$$

$$\Delta\ddot{y} = -2(\Omega c)\Delta\dot{x} + u_y \tag{5}$$

$$\Delta\ddot{z} = -q^2\Delta z + 2lq\cos(qt + \varnothing) + u_z \tag{6}$$

where Ω is the constant angular velocity of the orbit of the chaser, $\boldsymbol{\Delta r} = [\Delta x, \Delta y, \Delta z]^T$ is the LVLH position of the target, $\boldsymbol{u} = [u_x, u_y, u_z]^T$ is the control input, and c is defined as

$$c = \sqrt{1 + \frac{3J_2R_{\oplus}^2}{8r_{ref}^2}\left(1 + 3\cos(2i_{ref})\right)} \tag{7}$$

where r_{ref} and i_{ref} are the radius and inclination of the orbit of the chaser. The parameters $\varnothing$, l and q in the decoupled out-of-plane equation of motion in (6) are defined in [5].

The LVLH coordinate system attached to the chaser spacecraft is defined with origin at its center of mass as follows: the unit vector $\boldsymbol{\Delta\hat{x}}$ points from the center of the Earth towards the origin of the system, the unit vector $\boldsymbol{\Delta\hat{z}}$ is aligned with the orbit angular momentum vector and the unit vector $\boldsymbol{\Delta\hat{y}}$ completes a right-hand Cartesian coordinate system.

2.2. Drag Maneuvering Device

The Drag Maneuvering Device (DMD) [27] originally designed at the University of Florida ADAMUS laboratory for spacecraft controlled re-entry [28, 29, 30], has also shown to have potential for spacecraft relative maneuvers [31, 19] and passive attitude stabilization [32, 33]. The device consists of four 3.7 meters long repeatedly deployable/retractable surfaces offset 90 degrees from each other and inclined 20 degrees and is mounted on the anti-ram face of a CubeSat spacecraft providing additional cross-sectional area up to 0.5 m^2, see Figure 1.

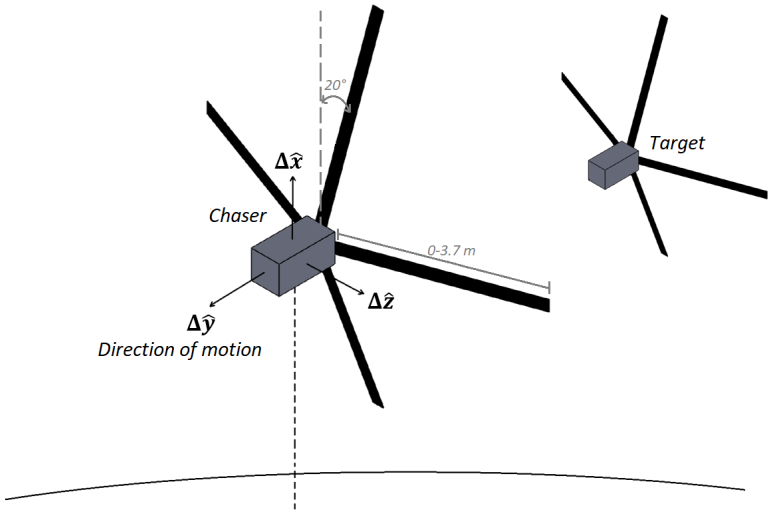

Figure 1: LVLH Coordinate System.

2.3. Differential Drag and Lift

Each maneuverable spacecraft in the fleet is capable of changing its experienced atmospheric drag and lift using the DMD. The contribution of each DMD surface on the atmospheric drag acceleration experienced by a spacecraft can be expressed as

$$\ddot{\boldsymbol{r}}_{\boldsymbol{D},\boldsymbol{j}} \triangleq -\frac{\rho(t) S C_{D,j}}{2m} V_r^2 \hat{\boldsymbol{V}}_{\boldsymbol{r}} \tag{8}$$

while the contribution on the lift acceleration is

$$\ddot{\boldsymbol{r}}_{\boldsymbol{L},\boldsymbol{j}} \triangleq -\frac{\rho(t) S C_{L,j}}{2m} V_r^2 \left(\hat{\boldsymbol{V}}_{\boldsymbol{r}} \times \hat{\boldsymbol{n}} \times \hat{\boldsymbol{V}}_{\boldsymbol{r}} \right) \tag{9}$$

where the subscript j indicates the j^{th} DMD surface on the spacecraft, $\rho(t)$ is the time-varying atmospheric density, $C_{D,j}$ is the drag coefficient, $C_{L,j}$ is the lift coefficient, $\hat{\boldsymbol{n}}$ is the the unit vector normal to the surface, S is the cross-sectional area of the surface, and m is the mass of the spacecraft. Therefore, a DMD-equipped spacecraft can change its experienced atmospheric drag and lift by varying S, i.e. extending/retracting the DMD surfaces. The vector $\boldsymbol{V}_{\boldsymbol{r}}$ represents the velocity of the spacecraft relative to the atmosphere which is assumed to be attached to the Earth and is defined as

$$\boldsymbol{V}_{\boldsymbol{r}} \triangleq \dot{\boldsymbol{r}} - \boldsymbol{\omega}_{\oplus} \times \boldsymbol{r} \tag{10}$$

where $\boldsymbol{\omega}_{\oplus}$ is the angular velocity of the Earth. The total experienced atmospheric drag and lift can then be computed by adding the contribution of all DMD surfaces mounted on the spacecraft as follows:

$$\ddot{\boldsymbol{r}}_{\boldsymbol{D}} = -\frac{\rho(t) S}{2m} V_r^2 \hat{\boldsymbol{V}}_{\boldsymbol{r}} \sum_{j=1}^{4} C_{D,j} \tag{11}$$

$$\ddot{\boldsymbol{r}}_{\boldsymbol{L}} = -\sum_{j=1}^{4} \frac{\rho(t) S C_{L,j}}{2m} V_r^2 \left(\hat{\boldsymbol{V}}_{\boldsymbol{r}} \times \hat{\boldsymbol{n}}_{\boldsymbol{j}} \times \hat{\boldsymbol{V}}_{\boldsymbol{r}} \right). \tag{12}$$

The drag and lift coefficients for the j^{th} surface mounted on a DMD-equipped spacecraft can be computed using the analytical expressions from [14, 15] which consider a flat plate in a free molecular flow:

$$C_{D,j} \triangleq \frac{2}{s\sqrt{\pi}} \exp\left(-s^2 \sin^2(\theta_{in})\right) + \frac{\sin(\theta_{in})}{s^2}(1+2s^2)\mathsf{erf}(s\sin(\theta_{in})) + \frac{\sqrt{\pi}}{s}\sin^2(\theta_{in})\sqrt{T_{k,out}/T_a} \tag{13}$$

$$C_{L,j} \triangleq \frac{\cos(\theta_{in})}{s^2}\mathsf{erf}(s\cos(\theta_{in})) + \frac{1}{s}\sqrt{\pi}\cos(\theta_{in})\sin(\theta_{in})\sqrt{T_{k,out}/T_a} \tag{14}$$

where $\mathsf{erf}(\cdot)$ represents the error function [34], $s = V_r\sqrt{m/(2k_BT_a)}$, k_B is the Boltzmann constant, θ_{in} is the principal rotation angle between $\hat{\boldsymbol{V}}_{\boldsymbol{r}}$ and $\hat{\boldsymbol{n}}$, T_a is the ambient atmosphere temperature, and $T_{k,out}$ is the reflected kinetic temperature of particles at the surface defined as

$$T_{k,out} \triangleq \frac{m}{3k_B}V_r^2(1-\alpha) + \alpha T_s \tag{15}$$

where T_s is the temperature of the surface, and α is an accommodation coefficient that represents the influence of the surface material properties. In this work the commonly used value of $\alpha = 0.9$ is adopted.

In a fleet with N chasers and one target, the differential atmospheric drag and lift between the i^{th} chaser and the target are given by

$$\boldsymbol{\Delta\ddot{r}_{D,i}} \triangleq \boldsymbol{\ddot{r}_{D,t}} - \boldsymbol{\ddot{r}_{D,i}} \tag{16}$$

$$\boldsymbol{\Delta\ddot{r}_{L,i}} \triangleq \boldsymbol{\ddot{r}_{L,t}} - \boldsymbol{\ddot{r}_{L,i}} \tag{17}$$

where the subscripts t and i represent the target and the i^{th} chaser, respectively.

3. Control Design

3.1. Control Objective

The control objective is to perform rendezvous and along-orbit formation maneuvers between a DMD-equipped spacecraft (chaser) and a target that could be either cooperative or unknown, using the differential drag as the control

input. The challenge of this problem is that the time-varying local atmospheric density $\rho(t)$, drag coefficients C_D and the magnitude of spacecraft-atmosphere velocity V_r are uncertain for both spacecraft. In addition, for the unknown target case, its area-to-mass ratio, e.g. the physical properties of the target, are also unknown. The following assumptions are made to simplify the control design process but are not used in the numerical simulations.

Assumption 2. Since the accommodation coefficient is $\alpha \approx 1$, the resulting lift coefficients C_L and accelerations $\ddot{\boldsymbol{r}}_{\boldsymbol{L}}$ are very small compared with those for drag. Therefore, the lift acceleration is neglected.

Assumption 3. The direction of each spacecraft-atmosphere relative velocity $\hat{\boldsymbol{V}}_{\boldsymbol{r}}$ is opposite to the $\boldsymbol{\Delta}\hat{\boldsymbol{y}}$ direction.

Considering Assumptions 2 and 3, the auxiliary control input in (4)-(6) can be written as

$$\boldsymbol{u} \triangleq \left(\rho_i(t) C_D^i V_{r,i}^2 \bar{u}(t) - \rho_t(t) V_{r,t}^2 \frac{C_D^t S_t}{2m_t}\right) \boldsymbol{\Delta}\hat{\boldsymbol{y}} \tag{18}$$

where $\bar{u} = S_i/(2m_i)$ represents the area-to-mass ratio of the i^th chaser spacecraft, which is the actual control input. The drag coefficient for the target C_D^t and for the i^{th} chaser C_D^i are defined as the summation of the drag coefficient of each DMD surface and are given by

$$C_D^k \triangleq \sum_{j=1}^{4} C_{D,j} \ , \quad k = t, i. \tag{19}$$

From the definition of $\boldsymbol{u}$, although the DMD surfaces on the target spacecraft could be maneuverable, meaning that S_t can also change for the cooperative case, the chaser will be the one responsible of achieving the required differential drag provided a known area-to-mass ratio $S_t/(2m_t)$ of the cooperative target or an estimate of this ratio for the unknown target. Also, given the direction of $\boldsymbol{u}$, its magnitude is given entirely in the component u_y as

$$u_y \triangleq \left(\rho_i(t) C_D^i V_{r,i}^2 \bar{u}(t) - \rho_t(t) V_{r,t}^2 \frac{C_D^t S_t}{2m_t}\right). \tag{20}$$

Inspired by the results in [35], where the differential drag was modeled as a time-varying function with its two principal Fourier components at 0 and Ω, and considering that the behavior over time of the differential in that case was dominated by the variation of the atmospheric density, this parameter can be modeled as

$$\rho_k(t) \triangleq D_{1,k} + D_{2,k}\sin(\Omega t) + D_{3,k}\cos(\Omega t)\,, \quad k = t, i \tag{21}$$

where $D_{1,k}$, $D_{2,k}$, $D_{3,k} \in \mathbb{R}$ are unknown constants.

3.2. Control Development

Considering that u_y is the only nonzero component of the auxiliary control input $\boldsymbol{u}$, and given that the out-of-plane ($\boldsymbol{\Delta z}$) dynamics are decoupled (see (4)-(6)), then only the in-plane motion can be affected by means of differential drag. The in-plane SS dynamics can be represented in state space form as

$$\underbrace{\begin{bmatrix} \Delta\dot{x} \\ \Delta\ddot{x} \\ \Delta\dot{y} \\ \Delta\ddot{y} \end{bmatrix}}_{\dot{\boldsymbol{X}}} = \underbrace{\begin{bmatrix} 0 & 1 & 0 & 0 \\ b & 0 & 0 & a \\ 0 & 0 & 0 & 1 \\ 0 & -a & 0 & 0 \end{bmatrix}}_{A} \underbrace{\begin{bmatrix} \Delta x \\ \Delta\dot{x} \\ \Delta y \\ \Delta\dot{y} \end{bmatrix}}_{\boldsymbol{X}} + \underbrace{\begin{bmatrix} 0 \\ 0 \\ 0 \\ 1 \end{bmatrix}}_{\boldsymbol{B}} u_y \tag{22}$$

where $a \triangleq 2\Omega c$ and $b \triangleq (5c-2)\Omega^2$ are known positive constants.

To compensate for the uncertain parameters in the auxiliary control input u_y, (20) can be linearly parameterized as

$$u_y = \boldsymbol{Y}\boldsymbol{\Theta}, \tag{23}$$

where $\boldsymbol{Y} \in \mathbb{R}^6$ denotes the measurable regression matrix

$$\boldsymbol{Y}(\bar{u}(t), \Omega) \triangleq \begin{bmatrix} \bar{u} & \bar{u}\sin(\Omega t) & \bar{u}\cos(\Omega t) & -\frac{S_t}{2m_t} & -\frac{S_t}{2m_t}\sin(\Omega t) & -\frac{S_t}{2m_t}\cos(\Omega t) \end{bmatrix} \tag{24}$$

and the vector of uncertain constant parameters $\boldsymbol{\Theta} \in \mathbb{R}^6$ is defined as

$$\boldsymbol{\Theta} \triangleq \begin{bmatrix} D_{1,i} C_D^i V_{r,i}^2 \\ D_{2,i} C_D^i V_{r,i}^2 \\ D_{3,i} C_D^i V_{r,i}^2 \\ D_{1,t} C_D^t V_{r,t}^2 \\ D_{2,t} C_D^t V_{r,t}^2 \\ D_{3,t} C_D^t V_{r,t}^2 \end{bmatrix}. \tag{25}$$

For the unknown target case, the area to mass ratio $S_t/(2m_t)$ can be moved from the regression matrix $\boldsymbol{Y}$ to the last three entries of the uncertain vector $\boldsymbol{\Theta}$, meaning that its entire ballistic coefficient $C_b^t = C_D^t S_t/(2m_t)$ is uncertain.

Since all the uncertain parameters in $\boldsymbol{\Theta}$ represent physical quantities, their entries can be upper and lower bounded as

$$\underline{\Theta}_j < \Theta_j < \bar{\Theta}_j \tag{26}$$

where Θ_j is the j^{th} entry of $\boldsymbol{\Theta}$, and $\underline{\Theta}_j, \bar{\Theta}_j \in \mathbb{R}$ denote the known bounds for the corresponding parameter. Similarly, the linear parameterization using the estimates is

$$\boldsymbol{Y}\hat{\boldsymbol{\Theta}} \triangleq \hat{\rho}_i(t)\hat{C}_D^i \hat{V}_{r,i}^2 \bar{u}(t) - \hat{\rho}_t(t)\hat{V}_{r,t}^2 \frac{\hat{C}_D^t S_t}{2m_t} \tag{27}$$

where $\hat{\boldsymbol{\Theta}} \in \mathbb{R}^6$ is the estimate of $\boldsymbol{\Theta}$, $\hat{\rho}_k(t) = \hat{D}_{1,k} + \hat{D}_{2,k}\sin(\Omega t) + \hat{D}_{1,k}\cos(\Omega t)$, and $\hat{D}_{1,k}, \hat{D}_{2,k}, \hat{D}_{3,k}, \hat{V}_{r,k}^2$ and $\hat{C}_D^k$ are estimates of $D_{1,k}, D_{2,k}, D_{3,k}, V_{r,k}^2$ and C_D^k, respectively. In case the target was unknown, the true values of S_t and m_t can be replaced by their estimates $\hat{S}_t$ and $\hat{m}_t$, respectively.

Let us define the estimation error $\tilde{\boldsymbol{\Theta}}$ as

$$\tilde{\boldsymbol{\Theta}} \triangleq \boldsymbol{\Theta} - \hat{\boldsymbol{\Theta}}. \tag{28}$$

Then, the auxiliary control input u_y can be rewritten as

$$u_y = \boldsymbol{Y}\tilde{\boldsymbol{\Theta}} + \boldsymbol{Y}\hat{\boldsymbol{\Theta}}. \tag{29}$$

To facilitate the subsequent stability analysis it will be useful to express the auxiliary control input as

$$u_y \triangleq u_{FB} + u_{AD}, \tag{30}$$

where $u_{FB}, u_{AD} \in \mathbb{R}$ are subsequently detailed state feedback and adaptation terms, respectively.

Using the SS dynamics in (22), it can be shown by evaluating the rank of the controllability matrix that the system is controllable using the auxiliary input u_y. Therefore, the state feedback term u_{FB} can be designed with the purpose of regulating the four states using a Linear Quadratic Regulator (LQR). The LQR provides a state feedback control law that regulates all states of the SS dynamics to zero while minimizing the cost function

$$J = \int_0^\infty \left(\boldsymbol{X}^T Q \boldsymbol{X} + R u_{FB}^2 \right) dt \tag{31}$$

where $\boldsymbol{X} \in \mathbb{R}^4$ is the measurable state vector defined in (22), $Q \in \mathbb{R}^{4\times4}$ is a positive definite weight matrix used to specify the desired performance of each state, and $R \in \mathbb{R}_{>0}$ is a weight used to penalize the control effort. The state feedback control law is defined as

$$u_{FB} = -\boldsymbol{K_{LQR}} \boldsymbol{X} \tag{32}$$

where $\boldsymbol{K_{LQR}} \in \mathbb{R}^4$ is a constant feedback gain vector that can be obtained from solving the Algebraic Riccati Equation (ARE) [36].

The approach of using a linear control technique such as the LQR is proposed taking advantage of the fact that all the nonlinearities and uncertainties are in the auxiliary control input. However, this control law by itself does not provide the adaptation capability required to compensate for the uncertain parameters. Therefore, the term u_{AD} is used for this purpose.

For simplicity, from this point on we will consider the more general case of an unknown target, the true values of S_t and m_t can be used instead whenever available. Using (29) and (30), substituting the definition of u_{FB} and solving

for u_{AD} yields

$$u_{AD} = \boldsymbol{Y}\tilde{\boldsymbol{\Theta}} + \hat{\rho}_i(t)\hat{C}_D^i \hat{V}_{r,i}^2 \bar{u}(t) - \frac{\hat{C}_D^t \hat{S}_t}{2\hat{m}_t}\hat{\rho}_t(t)\hat{V}_{r,t}^2 + \boldsymbol{K_{LQR}}\boldsymbol{X}. \tag{33}$$

Based on (32), (33), and the subsequent stability analysis, the control input $\bar{u}$ is designed as

$$\bar{u} \triangleq \left(\hat{\rho}_i(t)\hat{C}_D^i \hat{V}_{r,i}^2\right)^{-1}\left(\frac{\hat{C}_D^t \hat{S}_t}{2\hat{m}_t}\hat{\rho}_t(t)\hat{V}_{r,t}^2 - \boldsymbol{K_{LQR}}\boldsymbol{X}\right). \tag{34}$$

The estimates in (34) are determined from the adaptive update law

$$\begin{aligned}\dot{\hat{\boldsymbol{\Theta}}} \triangleq \mathsf{proj}\Bigg(&2\Gamma \boldsymbol{Y^T B^T} P^T \boldsymbol{X} \\ &+ \Gamma K_{ICL}\sum_{i=1}^{N_s} \mathcal{Y}_i^T \boldsymbol{B}^T\left(\boldsymbol{X}(t) - \boldsymbol{X}(t-\Delta t) - \mathcal{U}_i - \boldsymbol{B}\mathcal{Y}_i\hat{\boldsymbol{\Theta}}\right)\Bigg)\end{aligned} \tag{35}$$

where $\mathsf{proj}(\cdot)$ is the continuous projection algorithm developed in [37] used here to keep $\hat{\boldsymbol{\Theta}}$ within the bounds shown in (26), $N_s \in \mathbb{Z}_{>0}$ is the number of input-output data pairs, Δt is the time between samples, $\boldsymbol{B} \in \mathbb{R}^4$ is defined in (22), $P \in \mathbb{R}^{4\times 4}$ is a symmetric positive definite matrix used in the subsequent stability analysis, $\Gamma \in \mathbb{R}^{6\times 6}$ is the adaptation gain, K_{ICL} is a symmetric positive definite gain matrix and $\mathcal{Y}_i$ and $\mathcal{U}_i$ are defined as

$$\mathcal{Y}_i(\Delta t, t_i) \triangleq \int_{t_i-\Delta t}^{t_i} \boldsymbol{Y}(\sigma)d\sigma, \tag{36}$$

$$\mathcal{U}_i(\Delta t, t_i) \triangleq \int_{t_i-\Delta t}^{t_i} A\boldsymbol{X}(\sigma)d\sigma. \tag{37}$$

The update law in (35) is motivated by ICL-based approach to formulate a finite excitation condition that can be used for parameter identification. Specifically, the first terms in (35) are typical gradient-based terms motivated by the Lyapunov analysis to compensate for the uncertain disturbances. The terms within the summation can be rewritten in an equivalent analysis form, as

$$\dot{\hat{\boldsymbol{\Theta}}} = \mathsf{proj}\left(2\Gamma \boldsymbol{Y^T B^T} P^T \boldsymbol{X} + \Gamma K_{ICL}\sum_{i=1}^{N_s} \mathcal{Y}_i^T \mathcal{Y}_i \tilde{\boldsymbol{\Theta}}\right). \tag{38}$$

This form of the update law indicates that if sufficient input-output data is collected, then the summation of the regression matrices will be positive definite, which, unlike the traditional PE condition, can be verified online. The excitation condition is given by the following assumption.

Assumption 4. The system is sufficiently excited over a finite duration of time $T \in \mathbb{R}_{>0}$ such that [25, 26]

$$\lambda_{min}\left\{\sum_{i=1}^{N_s} \mathcal{Y}_i^T \mathcal{Y} i\right\} > \bar{\lambda} \quad \forall\, t \geq T \tag{39}$$

where $\lambda_{min}\{\cdot\}$ is the minimum eigenvalue of the matrix represented by the expression in $\{\cdot\}$, and $\bar{\lambda} \in \mathbb{R}_{>0}$ is a threshold defined by the user.

4. Stability Analysis

For the stability analysis two theorems are formulated. The first theorem shows the behavior of the system before the condition of finite excitation (Assumption 4) is satisfied, and the second theorem considers the system performance after satisfying this condition.

Theorem 1. Given the relative dynamics in (22) along with the adaptive update law in (38), the controller designed in (34) ensures that the estimation error $\tilde{\boldsymbol{\Theta}}$ remains bounded and the states $\boldsymbol{X}$ are asymptotically regulated in the sense that

$$\lim_{t\to\infty} \| \boldsymbol{X} \| = 0. \tag{40}$$

Proof. Let $t \in [0, T)$ and $V : \mathbb{R} \to \mathbb{R}_{\geq 0}$ be a candidate Lyapunov function defined as

$$V(\boldsymbol{\eta}) \triangleq \boldsymbol{X}^T P \boldsymbol{X} + \frac{1}{2} \tilde{\boldsymbol{\Theta}}^T \Gamma^{-1} \tilde{\boldsymbol{\Theta}}, \tag{41}$$

where the composite state vector $\boldsymbol{\eta} \in \mathbb{R}^{10}$ is

$$\boldsymbol{\eta} \triangleq \begin{bmatrix} \boldsymbol{X}^T & \tilde{\boldsymbol{\Theta}}^T \end{bmatrix}^T. \tag{42}$$

The candidate Lyapunov function can be bounded by

$$\beta_1 \parallel \boldsymbol{\eta} \parallel^2 \leq V(\boldsymbol{\eta}) \leq \beta_2 \parallel \boldsymbol{\eta} \parallel^2, \tag{43}$$

where β_1 and β_2 are positive bounding constants.

Substituting (22), (30) and (32) into the time derivative of (41) yields

$$\dot{V}(\boldsymbol{\eta}) = \boldsymbol{X}^T(PA^* + A^{*T}P)\boldsymbol{X} + 2\boldsymbol{X}^T P\boldsymbol{B}u_{AD} - \tilde{\boldsymbol{\Theta}}^T\Gamma^{-1}\dot{\hat{\boldsymbol{\Theta}}}, \tag{44}$$

where $A^* \triangleq A - \boldsymbol{B}\boldsymbol{K_{LQR}}$ and $A \in \mathbb{R}^{4\times 4}$ is defined in (22). Note that A^* is Hurwitz since $\boldsymbol{K_{LQR}}$ is obtained from solving the LQR problem. Therefore, a symmetric positive definite matrix $Q_1 \in \mathbb{R}^{4\times 4}$ can be determined so that

$$PA^* + A^{*T}P = -Q_1. \tag{45}$$

Substituting (33), (34) and (38) into the time derivative of the Lyapunov function yields

$$\dot{V}(\boldsymbol{\eta}) = -\boldsymbol{X}^T Q_1 \boldsymbol{X} - \tilde{\boldsymbol{\Theta}}^T K_{ICL} \sum_{i=1}^{N_s} \mathcal{Y}_i^T \mathcal{Y}_i \tilde{\Theta}. \tag{46}$$

Since $\sum_{i=1}^{N_s} \mathcal{Y}_i^T \mathcal{Y}_i$ is at least positive semi-definite for $t < T$, then (46) can be upper bounded by

$$\dot{V}(\boldsymbol{\eta}) \leq -\boldsymbol{X}^T Q_1 \boldsymbol{X}. \tag{47}$$

From (47), $\dot{V}$ is negative semi-definite, indicating that $V \in \mathcal{L}_\infty$. Therefore, $\boldsymbol{X}, \tilde{\boldsymbol{\Theta}} \in \mathcal{L}_\infty$, and then $\boldsymbol{\eta} \in \mathcal{L}_\infty$. Using (28), $\hat{\boldsymbol{\Theta}} \in \mathcal{L}_\infty$. Since $\sin(\Omega t), \cos(\Omega t) \in \mathcal{L}_\infty$ by definition, then the estimated atmospheric density $\hat{\rho}_i(t), \hat{\rho}_t(t) \in \mathcal{L}_\infty$. Therefore, from (34), $\bar{u} \in \mathcal{L}_\infty$. Since $\bar{u} \in \mathcal{L}_\infty$, then $\boldsymbol{Y} \in \mathcal{L}_\infty$ from (24), and then $\dot{\boldsymbol{X}} \in \mathcal{L}_\infty$ from (22). Since $\dot{\boldsymbol{X}} \in \mathcal{L}_\infty$, then $\boldsymbol{X}$ is uniformly continuous and from (47), $\boldsymbol{X} \in \mathcal{L}_2$. Therefore, by Barbalat's lemma [38]

$$\lim_{t\to\infty} \parallel \boldsymbol{X} \parallel = 0. \tag{48}$$

Now, the performance improvement after satisfying the finite excitation condition is described through Theorem 2.

Theorem 2. Given the relative dynamics in (22) along with the adaptive update law in (38), the controller designed in (34) yields exponential regulation of the states $\boldsymbol{X}$ and estimation error $\tilde{\boldsymbol{\theta}}$ in the sense that

$$\| \boldsymbol{\eta}(t) \| \leq \frac{\beta_2}{\beta_1} \mathsf{exp}\left(\frac{\lambda}{2\beta_2} T\right) \| \boldsymbol{\eta}(0) \| \, \mathsf{exp}\left(-\frac{\lambda}{2\beta_2} t\right) \tag{49}$$

for all $t \in [0, \infty)$, where

$$\lambda \triangleq \mathsf{min}\left\{ \lambda_{min}\left\{Q_1\right\}, \lambda_{min}\left\{ K_{ICL} \sum_{i=1}^{N_s} \mathcal{Y}_i^T \mathcal{Y}_i \right\} \right\}. \tag{50}$$

Proof. When $t > T$, the term $\sum_{i=1}^{N_s} \mathcal{Y}_i^T \mathcal{Y}_i$ becomes positive definite under Assumption 4. Therefore, (46) can be upper bounded by

$$\dot{V}(\boldsymbol{\eta}) \leq -\lambda_{min}\left\{Q_1\right\} \| \boldsymbol{X} \|^2 - \lambda_{min}\left\{ K_{ICL} \sum_{i=1}^{N_s} \mathcal{Y}_i^T \mathcal{Y}_i \right\} \| \tilde{\boldsymbol{\Theta}} \|^2, \tag{51}$$

which can be rewritten as

$$\dot{V}(\boldsymbol{\eta}) \leq -\lambda \| \boldsymbol{\eta} \|^2 . \tag{52}$$

Using the Comparison Lemma from [38] and (43) yields

$$V(\boldsymbol{\eta}(t)) \leq V(\boldsymbol{\eta}(T)) \mathsf{exp}\left(-\frac{\lambda}{\beta_2}(t - T)\right) \quad \forall \, t \geq T, \tag{53}$$

and applying (43) to (53) we get

$$\| \boldsymbol{\eta}(t) \| \leq \sqrt{\frac{\beta_2}{\beta_1}} \| \boldsymbol{\eta}(T) \| \, \mathsf{exp}\left(-\frac{\lambda}{2\beta_2}(t - T)\right) \quad \forall \, t \geq T. \tag{54}$$

Moreover, from (47) we know that

$$V(\boldsymbol{\eta}(T)) \leq V(\boldsymbol{\eta}(0)) \tag{55}$$

which, using the bounds in (43), can be rewritten as

$$\beta_1 \| \boldsymbol{\eta}(T) \|^2 \leq \beta_2 \| \boldsymbol{\eta}(0) \|^2 . \tag{56}$$

Therefore

$$\| \boldsymbol{\eta}(T) \| \leq \sqrt{\frac{\beta_2}{\beta_1}} \| \boldsymbol{\eta}(0) \| . \tag{57}$$

Finally, substituting (57) into (54) yields

$$\| \boldsymbol{\eta}(t) \| \leq \frac{\beta_2}{\beta_1} \exp\left(\frac{\lambda}{2\beta_2} T\right) \| \boldsymbol{\eta}(0) \| \exp\left(-\frac{\lambda}{2\beta_2} t\right) \quad \forall\, t \geq 0, \tag{58}$$

which is an exponential envelope valid for $t \in [0, \infty)$.

5. Multiple Spacecraft Maneuvers

5.1. Rendezvous

When multiple chasers are maneuvering with respect to a single target, a given chaser-target pair can be treated as a set of SS equations where the in-plane states are required to be regulated. The adaptive control law in (34) has been designed to do that between two spacecraft, namely the target and the i^{th} chaser. The developed control law requires knowledge of the area-to-mass ratio of the target spacecraft and measurement of the relative states to compute the required cross-sectional area for the chaser spacecraft.

The multiple spacecraft scenario is then proposed as follows: In case a cooperative target is considered, one of the spacecraft in the fleet is selected as the target, this spacecraft broadcasts its ECI states and the current level of deployment of its DMD surfaces to all the chasers. When the target is unknown, each chaser is assumed capable of measuring the relative states of the target, and the estimates of S_t and m_t are included in $\hat{\boldsymbol{\Theta}}$ so that the control law (34) could be computed. Each chaser spacecraft determines its required cross-sectional area by evaluating (34) on-board and numerically propagating the parameter estimates $\hat{\boldsymbol{\Theta}}$. Note that at any time, in case the cooperative target spacecraft fails, any functional chaser can be labeled as the target and the control algorithm running on each remaining chaser can be re-initialized to maneuver with respect to the new target.

5.2. Along-orbit Formation

The along-orbit formation considers a fleet of multiple chasers and one target where the chasers are required to be along the orbit of the target with specific separations (Δd).

5.2.1. Change of Reference Frame

In the rendezvous problem, the LVLH reference frame with origin at the center of mass of the i^{th} chaser was used to compute the relative states. For the along-orbit formation, let us now consider a reference frame that has a position offset with respect to each LVLH but still moves with the corresponding chaser. A desired along-orbit distance with respect to the target Δd_i is given to the i^{th} chaser. This distance needs to be consistent with the assumptions made in the SS dynamics. Note that for the along-orbit formation case the distance Δd_i can be expressed as an offset in true anomaly $\Delta\nu_i$ with respect to that of the i^{th} chaser spacecraft as

$$\Delta\nu_i = \frac{\Delta d_i}{a_i}[\mathsf{rad}] \tag{59}$$

where a_i is the semi-major axis of the i^{th} chaser, then the orbital elements for the origin of the new reference frame are the same as those of the chaser but adding the offset $\Delta\nu_i$ to the true anomaly. The i^{th} coordinate system is defined by the $\boldsymbol{\Delta\hat{x}_i}$ axis pointing from the center of the earth towards the origin of the system (desired position for the i^{th} chaser), the $\boldsymbol{\Delta\hat{z}_i}$ axis aligned with the orbit angular momentum vector and the $\boldsymbol{\Delta\hat{y}_i}$ axis completing a right-hand Cartesian coordinate system as shown in Figure 2.

Each set of SS equations represent relative states with respect to the desired along-orbit position and the control goal remains the same as in the rendezvous case, i.e. regulate all states to zero. Therefore, the adaptive control law developed in Section 3 is still valid to perform the along-orbit formation maneuver.

5.2.2. Collision Risk Reduction

The presence of multiple spacecraft maneuvering at relatively small distances increases the risk of possible collisions, especially for rendezvous maneuvers. Having the same controller driving each chaser to the rendezvous state with respect to the target yields a similar behavior in the relative path that a chaser follows to reach it, and given the state feedback term in the control law it is

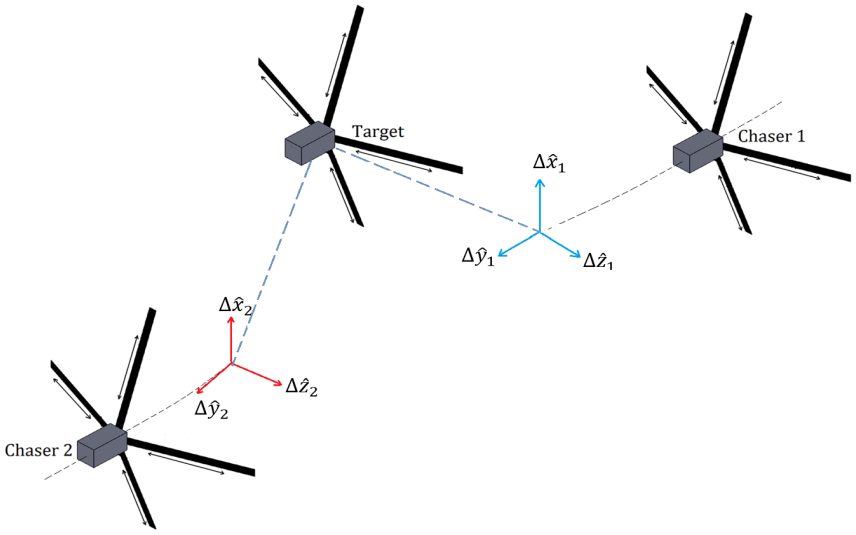

Figure 2: Modified Coordinate Systems.

expected that the control effort is reduced as the chaser approaches the target. Therefore, if a rendezvous maneuver is required, some chasers could follow similar paths and will be maneuvering in close proximity to the target for a significant portion of the maneuver, increasing the collision risk.

To reduce the collision risk, this undesired behavior could be addressed by introducing an along-orbit formation as an intermediate stage where the Δd_i's represent "parking" positions. Then, once the positions of the chasers are stable along the same orbit, the Δd_i's can be sequentially reduced to drive each chaser to the rendezvous state in a more controlled way when in close proximity to the target.

6. Simulation Results

To validate the adaptive controller designed in Section 3, a rendezvous maneuver with respect to a known target and an along-orbit formation with respect to an unknown target are numerically simulated, both involving six chasers. The

number of spacecraft has been selected so that the plots showing the results are readable. Nevertheless, the algorithm does not change when scaling the size of the fleet. In all simulations the dynamics of each spacecraft are individually simulated using (1)-(3), and the real (unknown for the controller) atmospheric density is obtained using the NRLMSISE-00 model to compute the drag and lift accelerations. The initial conditions are selected such that the target spacecraft is in a circular orbit similar to that of the International Space Station (ISS), see Table 1. The initial conditions of the chasers are randomly generated by varying the semi-major axis a_t, eccentricity e_t and true anomaly ν_t of the target so that the inter-spacecraft distance satisfies Assumption 1, while the RAAN (Ω_t), argument of perigee (ω_t) and orbit inclination (i_t) remain unchanged for all spacecraft. The bounds for such variations are $a_i = a_t \pm 500$[m], $e_i = e_t + 3 \times 10^{-5}$, and $\nu_i = \nu_t \pm 0.2$ [deg], respectively.

a_t $[km]$	e_t	i_t $[deg]$	Ω_t $[deg]$	ω_t $[deg]$	ν_t $[deg]$
6.7281×10^3	0	51.94	206.36	101.07	108.08

Table 1: Initial conditions for the target spacecraft

The gain $\boldsymbol{K_{LQR}}$ was computed using the *lqr* command in Matlab with the SS dynamics. The values for the matrices Q and R are shown in Table 2. The solution of the ARE is used for P and the adaptive gain Γ is also shown in Table 2. The control parameters associated with the ICL portion are shown in Table 3. The physical parameters for all spacecraft are identical (Table 4) and the values for T_a and T_s required to compute the drag (unknown for the controller) and lift coefficients are those used in [15]. The initial guess for $\hat{\boldsymbol{\Theta}}$ is $\hat{\boldsymbol{\Theta}}_{\mathbf{0}} = [6.8, 0, 0, 6.8, 0, 0]^T \times 10^{-4}$ and $\hat{\boldsymbol{\Theta}}_{\mathbf{0}} = [6.8, 0, 0, 1.1, 0, 0]^T \times 10^{-4}$ for the cases with cooperative and unknown target, respectively.

Parameter	Known target	Unknown Target
Q	$\mathsf{diag}(30, 1, 3, 2)$	$\mathsf{diag}(180, 1, 1.8, 1)$
R	5×10^{15}	6×10^{16}
Γ $(\times 10^{-20})$	$\mathsf{diag}(45, 15, 15, 45, 15, 15)$	$\mathsf{diag}(30, 30, 30, 0.3, 0.3, 0.3)$

Table 2: Controller parameters. Two sets of gains are presented, one for the case of a cooperative target and the other for maneuvers with respect to an unknown target

Parameter	Known Target	Unknown Target
$\bar{\lambda}$	400	500
K_{ICL} $(\times 10^{10})$	$\mathsf{diag}(3, 30, 30, 3, 30, 30)$	$\mathsf{diag}(5, 100, 100, 10, 80, 80)$

Table 3: Controller parameters for the ICL portion. Two sets of gains are presented, one for the case of a cooperative target and the other for maneuvers with respect to an unknown target

$S_t,\ S_i\ [m^2]$	$m_t,\ m_i\ [kg]$	$S_{t,max},\ S_{i,max}\ [m^2]$	$S_{t,min},\ S_{i,min}\ [m^2]$
0.2	1.5	0.5	0.01

Table 4: Spacecraft physical parameters. To simulate the unknown target, the same physical parameters were used to propagate its dynamics but are unknown for the controller.

6.1. Rendezvous Maneuver Results

For the rendezvous maneuver, the target spacecraft is assumed to be known and independently maneuvering its drag surfaces. However, it broadcasts its current cross-sectional area to all chasers. Figure 3 shows each in-plane relative state as a function of time. The controller required 120 hours to drive all chasers to the rendezvous state. The maneuver time was computed as the time that all chasers required to enter and remain inside a circle with radius 20 meters around the target.

The cross-sectional area that all the spacecraft required to perform the rendezvous maneuver are shown in Figure 4. Although the R matrix in the LQR

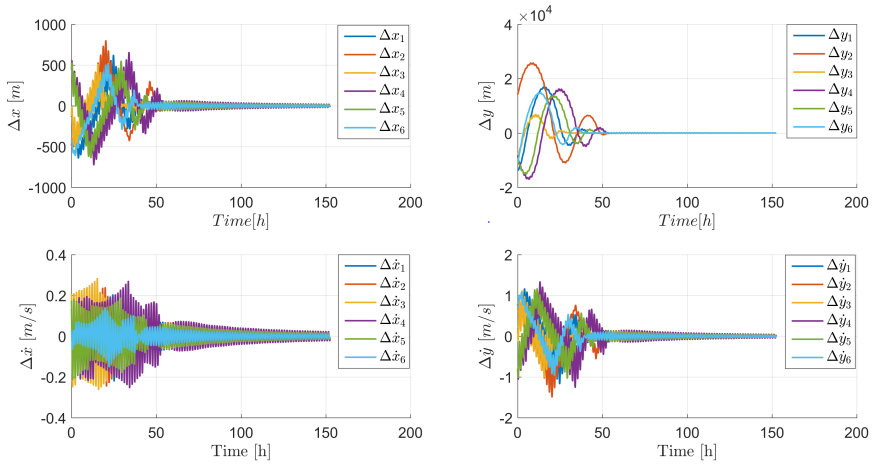

Figure 3: In-plane relative states as function of time for the rendezvous maneuver. The relative states are regulated between each chaser/target pair in 120 hours.

problem has a high value to reduce the required control effort, saturation was applied to the cross-sectional area of each spacecraft to ensure that the applied control inputs are always within the physical limits.

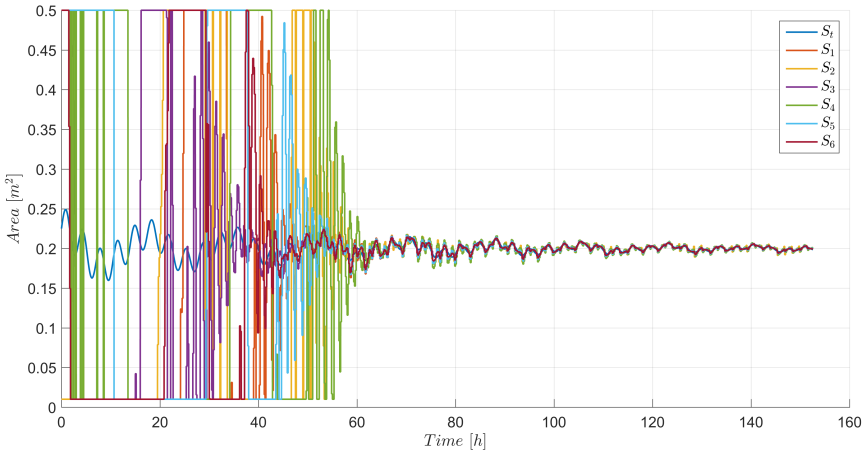

Figure 4: Cross-sectional areas required for the rendezvous maneuver. The control input $\bar{u}$ is saturated to ensure that the cross-sectional area does not exceed the physical limits of the DMD.

To reduce the possibility of having maneuvers where the threshold $\bar{\lambda}$ was not reached by any chaser, a relatively small value is set for this parameter. Additionally, to keep improving the convergence rate of the estimations when possible, the ICL portion of the adaptive update law is updated with new input-output data pairs every time $\lambda_{min}\left\{\sum_{i=1}^{N_s}\mathcal{Y}_i^T\mathcal{Y}_i\right\}$ increases, even after time $t=T$. The resulting behavior of these eigenvalues is shown in Figure 5.

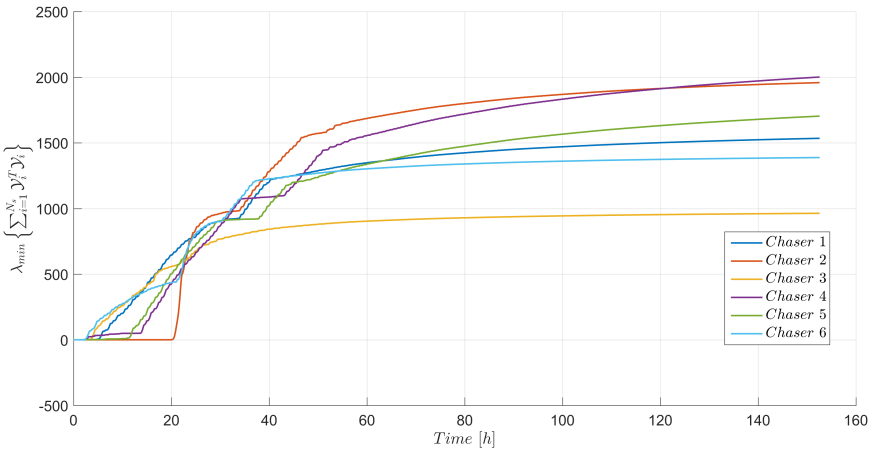

Figure 5: Behavior of each $\lambda_{min}\left\{\sum_{i=1}^{N_s}\mathcal{Y}_i^T\mathcal{Y}_i\right\}$ for the rendezvous maneuver. Threshold set to $\bar{\lambda}=400$, input-output data added after $t>T$ to improve convergence rate when possible.

The behavior over time of the vector $\hat{\boldsymbol{\Theta}}$ is shown component-wise in Figures 6 and 7 for parameters associated with the chasers and the target, respectively. Since all the chasers satisfied condition (39), these results indicate that there is a higher level of agreement in the estimations of the first and fourth entries of $\hat{\boldsymbol{\Theta}}$. These two entries are the most important parameters given that they are associated with the zero frequency level of the atmospheric density ($D_{1,i}$ and $D_{1,t}$) which are in general greater than those associated with the frequency Ω ($D_{2,i}, D_{2,t}, D_{3,i}$ and $D_{3,t}$). The small differences in the values of convergence can be attributed to the approximation made when modeling the density as in (21) and using the approximated SS relative dynamics.

The comparison between the real parameters ($\rho_k C_D^k V_{r,k}^2,\ k = i, t$) and the reconstruction of the estimated parameters ($\hat{\rho}_k \hat{C}_D^k \hat{V}_{r,k}^2,\ k = i, t$) are shown in Figures 8-11. These results show that the ICL-based controller is capable of adjusting the parameters to approximate their real values. The algorithm provides useful information about the uncertain parameters without relying on highly complex atmospheric models, forecasts and/or iterative algorithms.

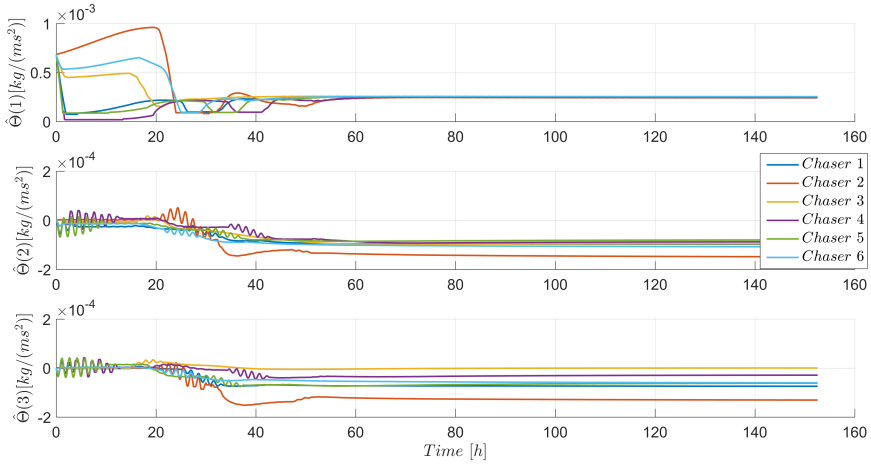

Figure 6: Behavior of estimations associated with each chaser over time for the rendezvous maneuver. Greater level of agreement can be observed in the estimations of $\hat{\Theta}(1) = D_{1,i} C_D^i V_{r,i}^2$, which in general has higher order of magnitude that the other two uncertain parameters associated with each chaser. Residual errors can be attributed to the approximations made during the controller design.

6.2. Along-Orbit Formation Results

For the along-orbit formation, the target spacecraft is assumed to be unknown. In this case, the chasers are required to perform an along-orbit formation centered on the target with inter-spacecraft separation of $1\ km$. The corresponding slot for each chaser, i.e. its $\Delta\nu_i$, was randomly selected. In addition to the individual nonlinear dynamics and the NRLMSISE-00 atmospheric model, a variation of $\pm 10\%$ with frequency of 1 RPM is applied to the bal-

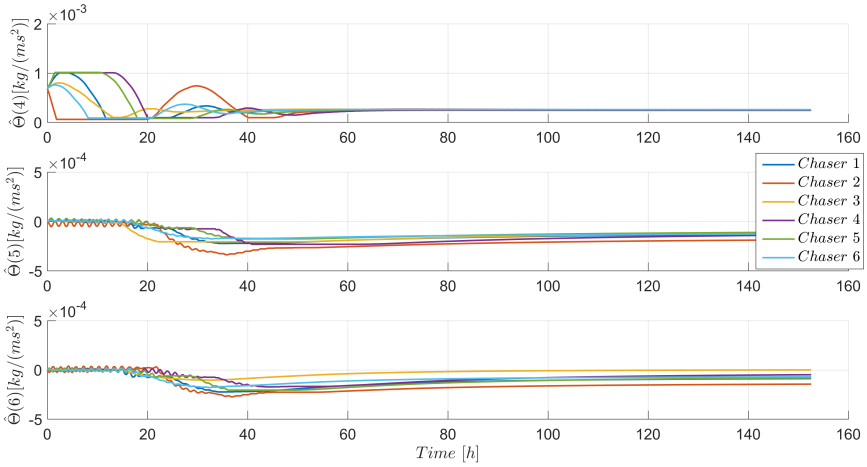

Figure 7: Behavior of estimations associated with the target over time for the rendezvous maneuver. Greater level of agreement can be observed in the estimations of $\hat{\Theta}(4) = D_{1,t}C_D^t V_{r,t}^2$, which in general has higher order of magnitude that the other two uncertain parameters associated with the Target. Residual errors can be attributed to the approximations made during the controller design.

listic coefficient C_b^t to simulate a tumbling unknown target. Figure 12 shows each in-plane relative state as a function of time. The maneuver time for the along-orbit formation maneuver was 100 hours. For convenience, the relative states have been plotted with respect to an LVLH coordinate system centered on the target so that the along-orbit separations (mostly along $\boldsymbol{\Delta\hat{y}}$) could be observed.

Although the chasers only modulate their cross-sectional areas S_i, the control inputs are plotted in Figure 13 as ballistic coefficients so that they can be compared to that of the unknown target. Saturation has also been applied to ensure the control inputs are within the bounds. The control inputs show that each chaser spacecraft has to keep maneuvering even after reaching its desired slot to compensate for the natural drifting with respect to the target.

The behavior of each $\lambda_{min}\left\{\sum_{i=1}^{N_s}\mathcal{Y}_i^T\mathcal{Y}_i\right\}$ is shown in Figure 14 and the behavior of $\hat{\boldsymbol{\Theta}}$ over time is shown in Figures 15 and 16 for parameters asso-

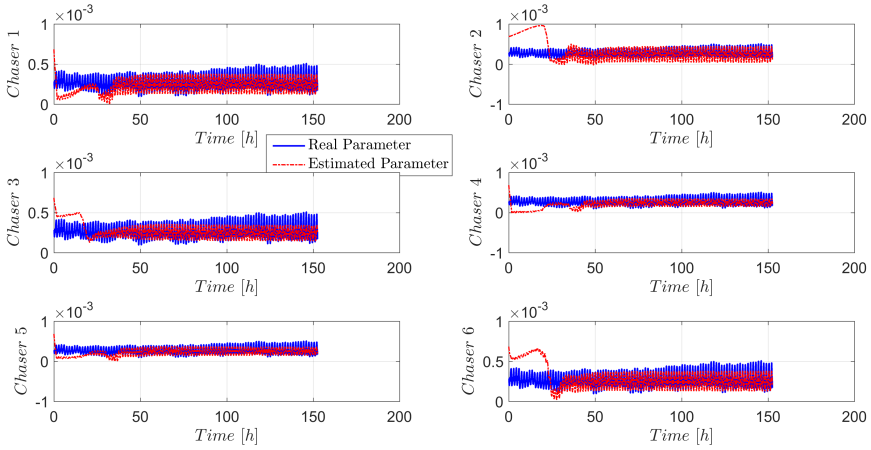

Figure 8: Real (solid blue line) vs reconstructed estimated parameters (dashed red line) associated with each chaser for the rendezvous maneuver. The real parameter was obtained using the NRLMSISE-00 atmospheric model. Amplitude in $[kg/(ms^2)]$.

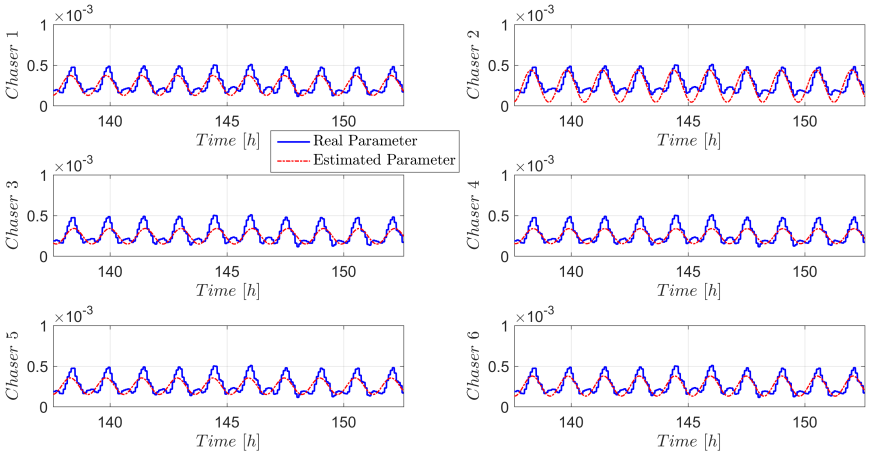

Figure 9: Zoomed-in view for the last 10 orbits of the real (solid blue line) vs reconstructed estimated parameters (dashed red line) associated with each chaser for the rendezvous maneuver. Amplitude in $[kg/(ms^2)]$.

ciated with each chaser and the target, respectively. Similar to the results for the rendezvous maneuver, the greatest estimation agreement is observed in the

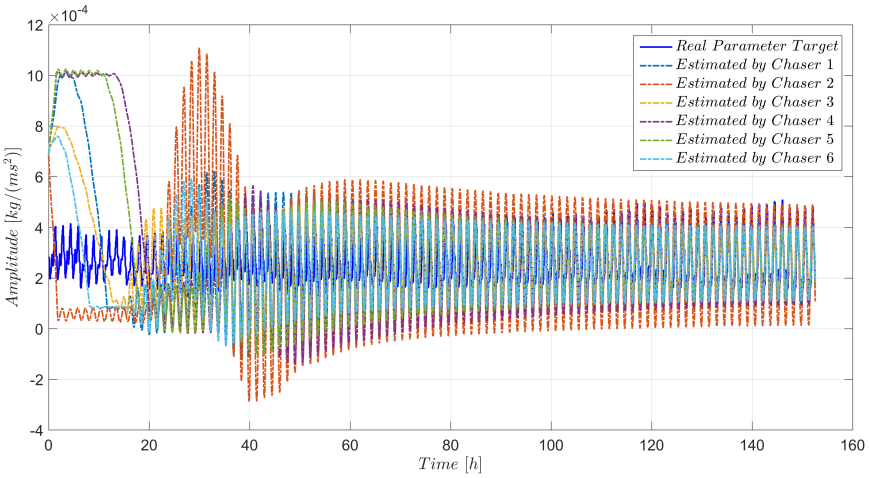

Figure 10: Real (solid blue line) vs reconstructed estimations (dashed lines) of the uncertain parameters of the target made by each chaser for the rendezvous maneuver. The real parameter was obtained using the NRLMSISE-00 atmospheric model.

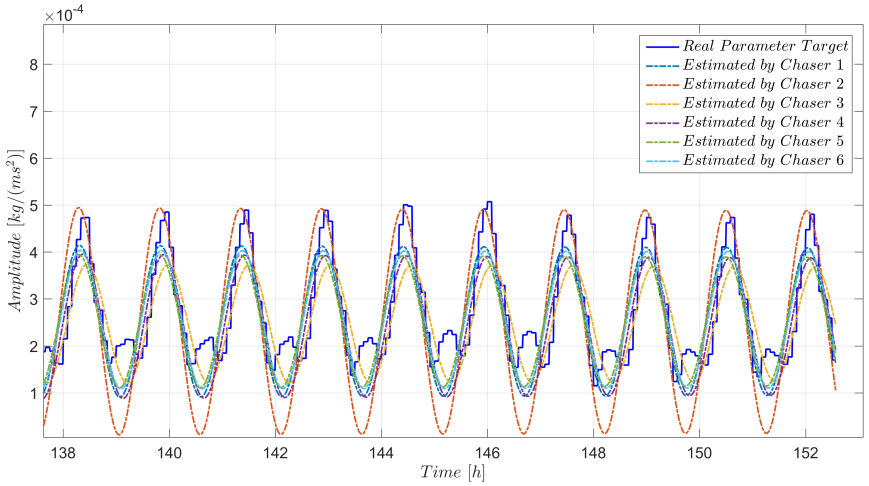

Figure 11: Zoomed-in view for the last 10 orbits of the real (solid blue line) vs reconstructed estimations (dashed lines) of the uncertain parameters of the target made by each chaser for the rendezvous maneuver.

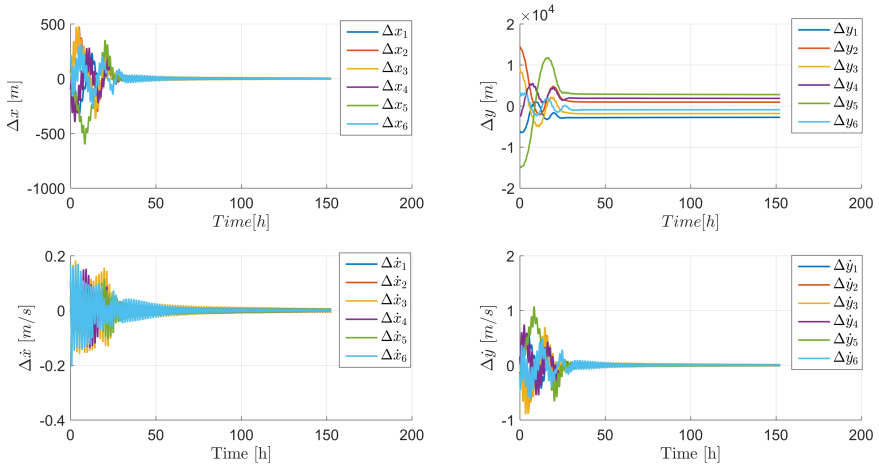

Figure 12: In-plane relative states as function of time for the along-orbit formation maneuver. The formation is achieved in 100 hours, inter-spacecraft separation of 1 km can be observed mainly in the Δy plot.

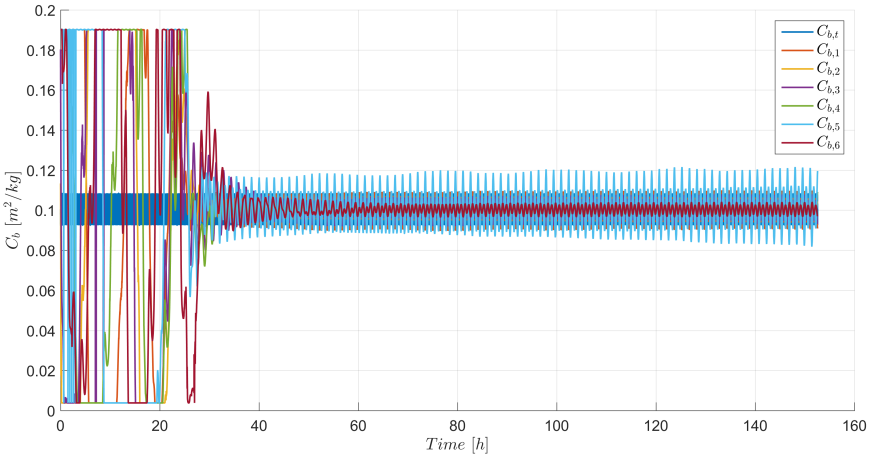

Figure 13: Ballistic coefficients required for the along-orbit formation maneuver. The control input $\bar{u}$ is saturated to ensure that the cross-sectional area does not exceed the physical limits of the DMD. Chasers need to keep maneuvering to maintain their desired relative positions.

parameters associated with the zero frequency of the atmospheric density. On the other hand, the estimated parameters associated with the frequency Ω show more disagreement between chasers.

The comparison between the real parameters $(\rho_i C_D^i V_{r,i}^2, \quad \rho_t C_b^t V_{r,t}^2)$ and the reconstruction of the estimated parameters $(\hat{\rho}_i \hat{C}_D^i \hat{V}_{r,i}^2, \quad \hat{\rho}_t \hat{C}_b^t \hat{V}_{r,t}^2)$ can be observed in Figures 17-20. The reduction in estimation performance compared to the cooperative target case can be attributed to the additional uncertainty in the physical parameters of the target and its tumbling behavior. Most of the performance reduction can be observed in the underestimation of the variations due to J_2 perturbation and day/night changes. However, the algorithm has shown estimation improvement from the *a priori* values of the uncertain parameters.

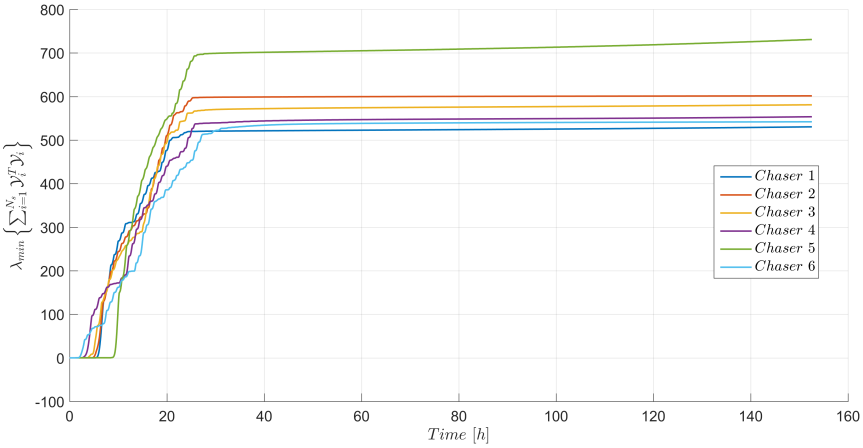

Figure 14: Behavior of each $\lambda_{min}\left\{\sum_{i=1}^{N_s} \mathcal{Y}_i^T \mathcal{Y}_i\right\}$ over time for the along-orbit formation maneuver. Threshold set to $\bar{\lambda} = 500$, input-output data added after $t > T$ to improve convergence rate when possible.

7. Conclusion

An ICL-based adaptive control strategy has been developed and validated for rendezvous and along-orbit formation maneuvers with respect to a single known

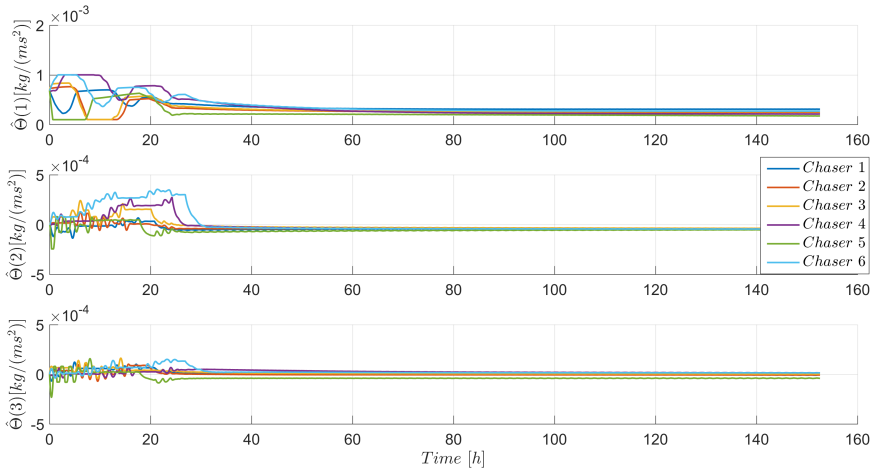

Figure 15: Behavior of estimations associated with each chaser over time for the along-orbit formation maneuver. Greater level of agreement can be observed in the estimations of $\hat{\Theta}(1) = D_{1,i}C_D^i V_{r,i}^2$, which in general has higher order of magnitude that the other two uncertain parameters associated with each chaser. Residual errors can be attributed to the approximations made during the controller design.

or unknown target. Numerical simulations demonstrate the performance of the developed controller. Parameters such as the local atmospheric densities, drag or ballistic coefficients and the magnitude of the spacecraft-atmosphere velocities are considered uncertain and the developed controller compensates for them. Additionally, when the system is sufficiently excited, the controller is able to estimate the values of these parameters on-line. The accuracy of the resulting parameter estimations have shown to be sufficient to determine their order of magnitude and the variations induced by the atmospheric density due to the J_2 perturbation and day/night changes. Errors in estimation can be attributed to the approximations made when modeling the atmospheric density, the use of the SS relative dynamics and (when unknown) the presence of a tumbling target. The developed algorithm is implementable on-board a CubeSat given that all the estimations are made online using simple integration algorithms without requiring large data sets nor computationally expensive operations.

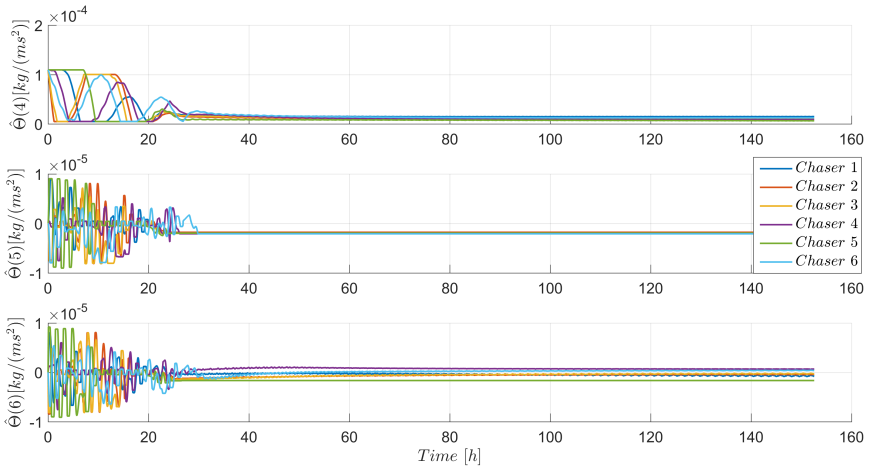

Figure 16: Behavior of estimations associated with the target over time for the formation maneuver. Greater level of agreement can be observed in the estimations of $\hat{\Theta}(4) = D_{1,t}C_b^t V_{r,t}^2$, which in general has higher order of magnitude that the other two uncertain parameters associated with the Target. Residual errors can be attributed to the approximations made during the controller design and the tumbling target.

8. Acknowledgments

This research has been supported by the Fulbright Colombia Commission and the AFOSR award number FA9550-19-1-0169. Any opinions, findings and conclusions or recommendations expressed in this material are those of the authors and do not necessarily reflect the views of the sponsoring agency.

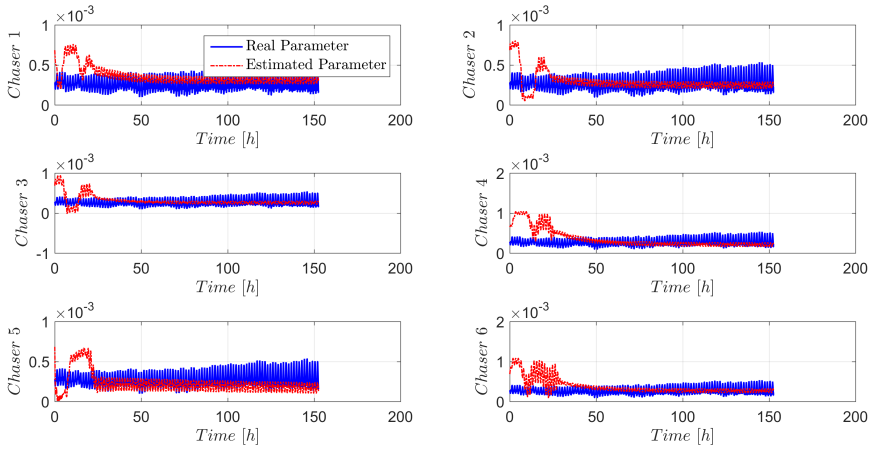

Figure 17: Real (solid blue line) vs reconstructed estimated parameters (dashed red line) associated with each chaser for the formation maneuver. The real parameter was obtained using the NRLMSISE-00 atmospheric model. Amplitude in $[kg/(ms^2)]$.

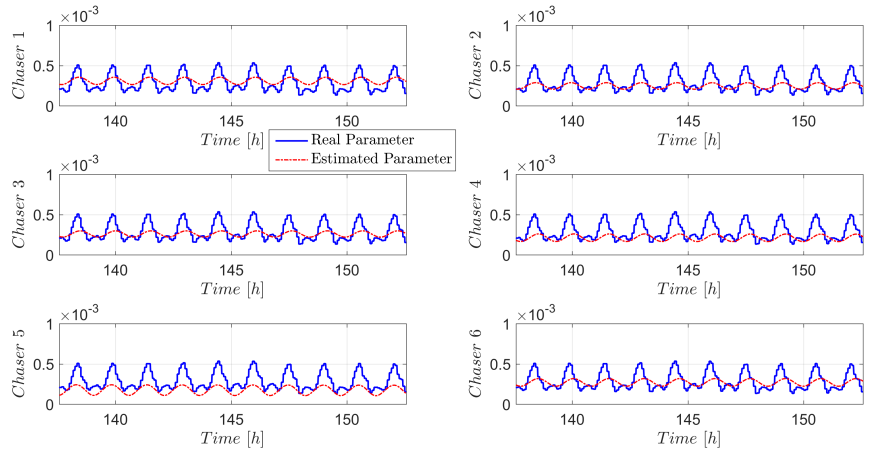

Figure 18: Zoomed-in view for the last 10 orbits of the real (solid blue line) vs reconstructed estimated parameters (dashed red line) associated with each chaser for the formation maneuver. Amplitude in $[kg/(ms^2)]$.

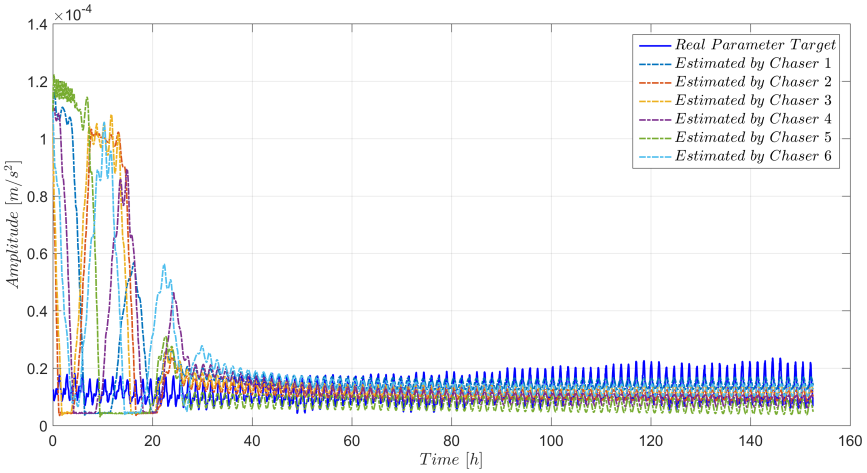

Figure 19: Real (solid blue line) vs reconstructed estimations (dashed lines) of the uncertain parameters of the target made by each chaser for the formation maneuver. The real parameter was obtained using the NRLMSISE-00 atmospheric model.

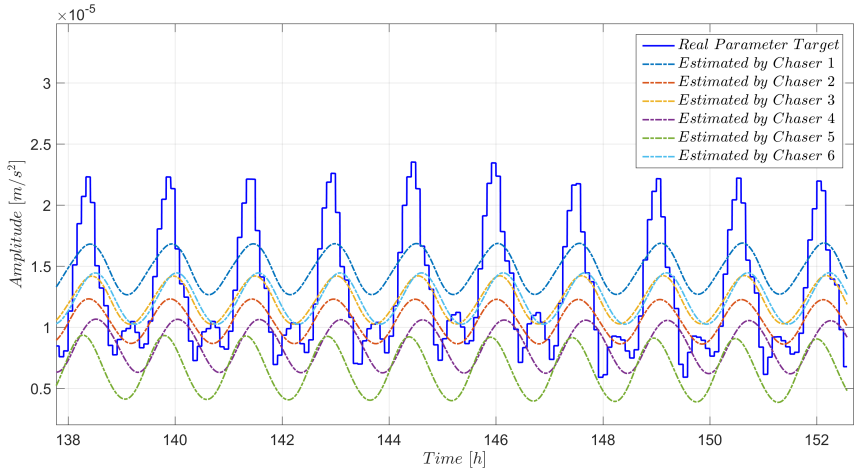

Figure 20: Zoomed-in view for the last 10 orbits of the real (solid blue line) vs reconstructed estimations (dashed lines) of the uncertain parameters of the target made by each chaser for the formation maneuver.

References

[1] T. D. Maclay, C. Tuttle, Satellite stationkeeping of the orbcomm constellation via active control of atmospheric drag: Operations, constraints and performance, Advances in the Astronautical Sciences 120 (1) (2005) 763–774.

[2] C. Foster, J. Mason, V. Vittaldev, L. Beukelaers, L. Stepan, R. Zimmerman, Constellation phasing with differential drag on planet labs satellites, Journal of Spacecraft and Rockets 55 (2) (2018) 473–483. doi:10.2514/1.A33927.

[3] C. L. Leonard, M. Hollister, E. V. Bergman, Orbital formationkeeping with differential drag, Journal of Guidance, Control and Dynamics 12 (1) (1989) 108–113. doi:10.2514/3.20374.

[4] M. Horsley, S. Nikolaev, A. Pertica, Rendezvous maneuvers of small spacecraft using differential lift and drag, Journal of Guidance, Control and Dynamics 36 (2) (2011) 445–453. doi:10.2514/1.57327.

[5] S. A. Schweighart, R. J. Sedwick, High-fidelity linearized j2 model for satellite formation flight, Journal of Guidance, Control and Dynamics 25 (6) (2002) 1073–1080. doi:10.2514/2.4986.

[6] R. Bevilacqua, M. Romano, Rendezvous maneuvers of multiple spacecraft by differential drag under j2 perturbation, Journal of Guidance, Control and Dynamics 31 (6) (2008) 1595–1607. doi:10.2514/1.36362.

[7] D. Perez, R. Bevilacqua, Differential drag spacecraft rendezvous using an adaptive lyapunov control strategy, Acta Astronautica 83 (2012) 196–207. doi:10.1016/j.actaastro.2012.09.005.

[8] D. Ivanov, M. Kushniruk, M. Ovchinnikov, Study of satellite formation flying control usign differential lift and drag, Acta Astronautica 152 (2018) 88–100. doi:10.1016/j.actaastro.2018.07.047.

[9] M. W. Harris, B. Açıkmeşe, Minimum time rendezvous of multiple spacecraft using differential drag, Journal of Guidance, Control and Dynamics 37 (2) (2014) 365–373. doi:10.2514/1.61505.

[10] S. Varma, K. D. Kumar, Multiple satellite formation flying using differential aerodynamic drag, Journal of Spacecraft and Rockets 49 (2) (2012) 325–336. doi:10.2514/1.52395.

[11] NOAA, U.s. standard atmosphere (1976) (1976).

[12] I. Harris, W. Priester, Time-dependent structure of the upper atmosphere, Journal of the Atmospheric Sciences 19 (4) (1962) 286–301. doi:10.1175/1520-0469(1962)019<0286:TDSOTU>2.0.CO;2.

[13] J. M. Picone, A. E. Hedin, D. P. Drob, A. C. Aikin, Nrlmsise-00 empirical model of the atmosphere: Statistical comparisons and cientific issues, Journal of Geophysical Research 107 (A12) (2002) 15–1–15–16. doi:10.1029/2002JA009430.

[14] M. Pilinskin, Dynamic gas-surface interaction modeling for satellite aerodynamic computations, Ph.D. thesis, University of Colorado Boulder (2011).

[15] A. Harris, H. Schaub, Differential lift and drag constellation control using trimmed attitude, in: AAS Spaceflight Mechanics Meeting, Maui, Hawaii, 2019, Paper No. AAS-19-431.

[16] D. D. Mazanek, R. R. Kumar, M. Qu, H. Seywald, Aerothermal analysis and design of the gravity recovery and climate experiment (grace) spacecraft (2000).

[17] P. M. Mehta, A. C. Walker, E. K. Sutton, H. C. Godinez, New density estimates derived using accelerometers on board the champ and grace satellites, Space Weather 15 (2017) 558–576. doi:10.1002/2016SW001562.

[18] O. Montenbruck, E. Gill, Satellite Orbits: Models, Methods and Applications, Springer, Berlin, 2000.

[19] C. Riano-Rios, R. Bevilacqua, W. E. Dixon, Adaptive control for differential drag-based rendezvous maneuvers with an unknown target, Acta Astronautica. To appear.

[20] K. S. Narendra, A. M. Annaswamy, Persistent excitation in adaptive systems, International Journal of Control 45 (1) (1987) 127–160. doi:10.1080/00207178708933715.

[21] G. Tao, Multivariable adaptive control: A survey, Automatica 50 (11) (2014) 2737–2764. doi:10.1016/j.automatica.2014.10.015.

[22] L. P. Perera, P. Oliveira, C. Guedes Soares, System identification of vessel steering with unstructured uncertainties by persistent excitation maneuvers, IEEE Journal of Oceanic Engineering 41 (3) (2016) 515–528. doi:10.1109/JOE.2015.2460871.

[23] G. Chowdary, Concurrent learning for convergence in adaptive control without persistency of excitation, Ph.D. thesis, Georgia Institute of Technology (2012).

[24] G. Chowdhary, T. Yucelen, M. Mühlegg, E. N. Johnson, Concurrent learning adaptive control of linear systems with exponentially convergent bounds disturbances, International Journal of Control and Signal Processing 27 (4) (2013) 280–301. doi:10.1002/acs.2297.

[25] A. Parikh, R. Kamalapurkar, W. E. Dixon, Integral concurrent learning: Adaptive control with parameter convergence using finite excitation, International Journal of Control and Signal Processing 33 (12) (2018) 1775–1787. doi:10.1002/acs.2945.

[26] Z. Bell, J. Nezvadovitz, A. Parikh, E. Schwartz, W. E. Dixon, Global exponential tracking control for an autonomous surface vessel: An integral concurrent learning approach, IEEE Journal of Oceanic Engineering 45 (2) (2020) 362–370. doi:10.1109/JOE.2018.2880622.

[27] D. Guglielmo, S. Omar, R. Bevilacqua, L. Fineberg, J. Treptow, B. Poffenberger, Y. Johnson, Drag de-orbit device: A new standard reentry actuator for cubesats, Journal of Spacecraft and Rockets 56 (1) (2018) 129–145. doi:10.2514/1.A34218.

[28] S. F. Rafano Carna, S. Omar, D. Guglielmo, R. Bevilacqua, Safety analysis for shallow controlled re-entries through reduced order modeling and inputs' statistics method, Acta Astronautica 155 (2018) 426–447. doi:10.1016/j.actaastro.2018.10.015.

[29] S. Omar, D. Guglielmo, R. Bevilacqua, Drag de-orbit device (d3) mission for validation of controlled spacecraft re-entry using aerodynamic drag, in: 4th IAA Dynamics and Control of Space Systems Conference, Rome, Italy., 2017.

[30] S. Omar, D. Guglielmo, G. Di Mauro, T. Martin, R. Bevilacqua, Cubesat mission to demosntrate aerodynamically controlled re-entry using the drag de-orbit device (d3), in: SmallSat Conference 2018, Logan, UT, 2018.

[31] C. Riano-Rios, R. Bevilacqua, W. E. Dixon, Relative maneuvering for multiple spacecraft via differential drag using LQR and constrained least squares, in: AAS Spaceflight Mechanics Meeting, Maui, Hawaii, 2019, Paper No. AAS-19-346.

[32] S. Omar, C. Riano-Rios, R. Bevilacqua, Semi-passive three axis attitude stabilization for earth observation satellites using the drag maneuvering device, in: 12th Symposium on Small Satellite for Earth Observation. Berlin, Germany. 2019, 2019.

[33] C. Riano-Rios, S. Omar, R. Bevilacqua, W. Dixon, Spacecraft attitude regulation in low earth orbit using natural torques, in: 2019 IEEE 4th Colombian Conference on Automatic Control (CCAC), Medellin, Colombia., 2019.

[34] C. W. Hall, Laws and Models: Science, Engineering and Technology, 1st Edition, CRC PRess, 2018.

[35] G. Gaias, J.-S. Ardaens, O. Montenbruck, Model of J2 perturbed satellite relative motion with time-varying differential drag, Celestial Mechanics and Dynamical Astronomy 123 (2015) 441–433. doi:10.1007/s10569-015-9643-2.

[36] J. P. Hespanha, Linear Systems Theory: Second Edition, Princeton University Press, 2018.

[37] W. E. Dixon, A. Behal, D. M. Dawson, S. Nagarkatti, Nonlinear Control of Engineering Systems: A Lyapunov-Based Approach, Birkhauser, Boston, 2003.

[38] H. K. Khalil, Nonlinear Systems, 3rd Edition, Prentice Hall, NJ, 2002.